Monthly Notices of the ROYAL ASTRONOMICAL SOCIETY

MNRAS **542,** 2363–2376 (2025) https://doi.org/10.1093/mnras/staf1383
Advance Access publication 2025 August 21

# Photochemical processing of $CH_4$:$O_2$ ices

Yanan Ge,[1] Congcong Zhang,[2★] Junfeng Zhen [2★] and Yuming Wang[1]

[1]*National Key Laboratory of Deep Space Exploration/School of Earth and Space Sciences, University of Science and Technology of China, Anhui, Hefei 230026, China*
[2]*Hunan Key Laboratory for Stellar and Interstellar Physics and School of Physics and Optoelectronics, Xiangtan University, Hunan, Xiangtan 411105, China*

Accepted 2025 August 18. Received 2025 August 12; in original form 2025 May 19

## ABSTRACT

During the star and planet formation, ultraviolet (UV) irradiation of ices on dust grain surfaces at low temperatures (∼10–20 K) is considered an efficient pathway for interstellar complex organic molecules (iCOMs) in the inter- and circumstellar medium (ISM/CSM). In this work, a series of laboratory experiments was performed to investigate the UV photoprocessing of binary ice mixtures ($CH_4$:$O_2$) under the simulated astrophysical environments. A variety of newly formed products, e.g. $CH_2O$, $CH_3OH$, $O_3$, CO, $CO_2$, $H_2O$, $H_2O_2$, HCOOH, $CH_3CH_2OH$, and $CH_3CHO$, are observed and identified after UV irradiation. In addition, the photoproduction rates of new species and the photodestruction cross-sections of $CH_4$/$CD_4$ are also obtained. These experimental results provide key information for understanding the photochemical processing of $CH_4$- and $O_2$-containing ices under astronomically relevant conditions. Furthermore, the observation of some organic compounds (e.g. $CH_2O$ and $CH_3OH$) and non-organic compounds (e.g. $O_3$ and $H_2O$) demonstrates that the ices of $CH_4$ and $O_2$ may play an essential role in the production of complex organic compounds and the evolution of circulated oxygen in space. Importantly, the formation reaction scheme of new species obtained here provides insight into the possible reaction pathways towards complex molecules observed from the ISM/CSM.

**Key words:** astrochemistry – molecular processes – methods: laboratory: solid state – ISM: molecules.

## 1 INTRODUCTION

Ices are abundantly present in dense interstellar cloud regions (Whittet et al. 1988). Cold and dense molecular clouds, such as the Taurus Molecular Cloud (TMC-1) and Bernard 68, are the birth sites of low- and high-mass stars and their planetary systems (Ehrenfreund & Charnley 2000). In general, dense interstellar clouds are characterized by high number densities (∼$10^4$ –$10^5$ $cm^{-3}$), low kinetic temperatures (∼10−20 K), and weak ultraviolet (UV) radiation fields ($A_V$ > 10 mag; van Dishoeck, Herbst & Neufeld 2013; Boogert, Gerakines & Whittet 2015). In molecular clouds, the life-forming elements (C, H, O, N, and S) that make up life are locked up in the ice mantles that cover the surface of dust grains (Gibb, Whittet & Chiar 2001; McClure, Rocha & Pontoppidan 2023). Furthermore, the column densities of the major and minor ice species indicate that ice contributes between 2 per cent and 19 per cent to the bulk budgets of the key elements C, O, N, and S (McClure et al. 2023). Most importantly, photochemistry in icy grain mantles is suggested as an efficiency path for chemical complexity (Greenberg & Hong 1974).

Oxygen is the third most abundant element in the universe and, therefore, its molecular form in different regions is of considerable astronomical importance (Savage & Sembach 1996; Asplund et al. 2009). Earlier gas-phase chemical models predict that $O_2$ and CO are the primary forms of elemental oxygen in dense molecular clouds (Herbst & Leung 1989; Millar & Herbst 1990; Wakelam, Herbst & Selsis 2006). So far, gaseous $O_2$ has been detected in two interstellar clouds with lower concentrations relative to $H_2$, namely, Orion ($O_2/H_2 \approx (0.3-7.3) \times 10^{-6}$, (Goldsmith et al. 2011; Chen et al. 2014)) and the star-forming region $\rho$ Ophiuchi A ($O_2/H_2 \approx 5 \times 10^{-8}$; Larsson et al. 2007; Liseau et al. 2012; Larsson & Liseau 2017). In the dense protostellar envelope, the upper limits of $O_2/H_2$ abundance as low as $6 \times 10^{-9}$ ($3\sigma$) have been reported (Yildiz et al. 2013). The isotopologue $^{16}O^{18}O$, with a dipole moment, has been tentatively detected in the protostellar system IRAS 16293-2422 B (Taquet et al. 2018).

Solid $O_2$ has not yet been detected in interstellar grains or protoplanetary discs. Solid $O_2$ has been searched but has not been detected in dense clouds due to its weak feature at 6.45 μm, and the derived results indicate that its abundance represents less than 6 per cent of the total oxygen budget in the ISM/CSM (Vandenbussche et al. 1999). The analysis for the solid $^{13}CO$ line profiles in the low- and high-mass star formation regions demonstrates that solid $O_2$ concentrations of less than 10 per cent with respect to $H_2O$ ice (Boogert, Blake & Tielens 2002; Pontoppidan et al. 2003).

$CH_4$ is among the simplest organic molecules and is an important reservoir for a large fraction of carbon on the grain surface (Garrod, Wakelam & Herbst 2007). Gas- and solid-phase $CH_4$ were first detected through its bending mode at 7.67 μm towards NGC 7538 IRS9 and probably W 33A, NGC 7538 IRS1 (Lacy et al. 1991). In addition, interstellar $CH_4$ was also identified toward Orion IRc2 through the space-based Infrared Space Observatory (ISO; de Graauw et al. 1996; van Dishoeck et al. 1998) and SOFIA/EXES

★ E-mail: zhangcongcong@mail.ustc.edu.cn (CZ); jfzhen@xtu.edu.cn (JZ)

(Nickerson et al. 2023). Later, ISO-SWS observations towards the deeply embedded protostellar objects W 33A and NGC 7538 IRS9 show a feature near 7.67 μm that is consistent with the absorption by solid $CH_4$ or the Q-branch of gaseous $CH_4$, and the column density of methane ice is low (1−2 per cent of $H_2O$ ice; $\sim10^{-6}$ of atomic H; Boogert et al. 1996, 1997, 1998; Boogert, Blake & Öberg 2004; Barentine J. & Lacy 2012).

The solid $CH_4$ abundance toward a large sample of low-mass young stellar objects is determined by infrared spectra from the Spitzer Space Telescope, and these results indicate that the solid $CH_4$ abundance with respect to $H_2O$ is centred at 5.8 per cent with a standard deviation of 2.7 per cent in these sources (Öberg & et 2008). In addition, $CH_4$ was also detected in the solid state in the Galactic centre (Chiar et al. 2000), an external galactic nucleus (Spoon et al. 2001), and comet C/2021 A1 (Leonard; Faggi et al. 2023). Relatively low-abundance methane has been proposed to be the starting point of rich interstellar chemistry, which leads to iCOMs in dense molecular clouds (Markwick, Millar & Charnley 2000; Dartois et al. 2005).

Research and reproduction of the process from simple ices to complex molecules is one of the most fundamental questions for the evolution of interstellar chemistry, especially grain surface chemistry (Gerakines P., Schutte W. & Ehrenfreund 1996; Öberg et al. 2009a, b; Öberg, van Dishoeck & Linnartz 2009c). Lamberts et al. (2017) focused on the quantum tunneling effects upon hydrogen abstraction in $CH_4$ + OH in the solid state, where OH radicals are produced by hydrogenation of $O_2$ in the ice, for example, $O_2 + H \rightarrow HO_2$ and $HO_2 + H \rightarrow OH + OH$ (Lamberts, de Vries & Cuppen 2014). Bergner, Öberg & Rajappan (2017) used a deuterium UV lamp to selectively dissociate $O_2$ within a mixture of $O_2$:$CH_4$ ices or $O_2$:$CH_4$:CO ices, and observed efficient production of $CH_3OH$ via O ($^1$D) insertion into $CH_4$. Chou et al. (2020) explored the photochemical behaviour of $CH_4$:$O_2$ mixed ices with UV photons generated by synchrotron radiation. In addition, previous studies have reported the photochemistry evolution of pure methane ice (Bossa et al. 2015; Dupuy et al. 2017; Carrascosa et al. 2020) and molecular oxygen ice (Gerakines et al. 1996; Raut et al. 2011; Zhen & Linnartz 2014) after UV irradiation.

Although many experimental and theoretical results have been studied, the reaction mechanisms that produce complex molecules during UV irradiation of most mixed ices remain poorly understood. In the case of experimental work on mixed $O_2$ and $CH_4$ mixed ices, limited work is available, and the presented work is also motivated by observations of $O_2$ gas in the ISM/CSM (Larsson et al. 2007; Goldsmith et al. 2011). In this article, we explore the photochemical processes of $CH_4$: $O_2$ mixed ices upon UV irradiation in simulated astrophysical environments.

## 2 EXPERIMENTAL METHODS

The experiments were performed in the CRYOPAD set-up, which has been described in detail before (Öberg et al. 2008). All experiments are carried out in the main chamber in an ultra-high vacuum environment (a base pressure on the order of $\sim10^{-10}$ mbar at room temperature). The Fourier Transform Infrared Spectrometer (FTIR) is used in reflection mode to detect the ice samples on the gold substrate. Table 1 summarizes the laboratory experiments carried out in this work.

In our experiments, $CH_4$, $CD_4$, and $O_2$ (Icon Isotopes, 99 per cent) samples are used. First, gas samples were continuously deposited on the gold substrate at 14–21 K by introducing gas-phase molecules into the chamber. For the gold substrate, the temperature was controlled to 14 K, which was monitored by a cryogenic temperature controller with an absolute accuracy of 2 K and a relative precision of 0.5 K. The thicknesses of these ices range from 8 to 80 monolayers (ML, 1 ML = $10^{15}$ molecules cm$^{-2}$), mostly with 40 ML. It is close to the thicknesses of ice that cover the surface of interstellar dust grains in the dense and cold stages of star formation. Moreover, the ice is so thick that photodesorption will not significantly affect the bulk of the ice based on previous research (Öberg et al. 2009b, c).

Subsequently, the ice samples were exposed to UV photons generated by the microwave discharge hydrogen lamp, peaks around Ly-$\alpha$ wavelengths with an energy extending between 6.0 and 11.5 eV (Muñoz Caro & Schutte 2003). All ices were irradiated by the UV light source for about 3 h, resulting in a total fluence of $\sim 1.0 \times 10^{18}$ photons cm$^{-2}$, which is comparable to the UV fluence in which ice in a cloud core is exposed to cosmic-ray-induced UV photons at a rate of $10^4$ cm$^{-2}$ s$^{-1}$ during $10^6$ yrs (Shen et al. 2004).

The original ice compositions were changed during UV irradiation. Following UV irradiation, IR spectra were collected every 5 min. The relative strengths of the IR band are consistent with the relative strengths of the transmission band in the investigated ice thickness regime and thus with the uncertainty within 20 per cent. The results of the analysis on the formation rates of products and the photodestruction cross-sections of the initial ices have been obtained and shown in Table 1. The photodestruction cross-section is defined as the effective interaction area averaged over the incident UV spectrum per target molecule per absorbed photon during the photodestruction process.

## 3 EXPERIMENTAL RESULTS AND ANALYSIS

Fig. 1 shows the overall IR spectra of different ices before and after UV irradiation with a UV fluence of $1.0 \times 10^{18}$ photons cm$^{-2}$. The pure ices are shown in left panels: (A1) 80 ML, 14 K, $CH_4$ ice; (A2) 40 ML, 14 K, $CD_4$ ice; (A3) 60 ML, 14 K, $O_2$ ice; The ice mixtures are shown in right panels: (B1) 80 ML, 14 K, $CH_4$:$O_2$ = 1:1 mixed ices; (B2) 50 ML, 14 K, $CD_4$:$O_2$ = 1:1 mixed ices; (B3) 80 ML, 14 K, $CH_4$:$CD_4$:$O_2$ = 1:1:2 mixed ices. In this figure, the coloured lines represent different ice samples exposed to UV irradiation, while the black lines represent ice without UV irradiation.

Upon irradiation, new absorption features are observed, indicating that new species are formed efficiently. As shown in Fig. 1, the IR characteristics of these ice species are mainly distributed between 900 and 2300 cm$^{-1}$. Thus, to better analyse the changes in the ice samples, we have plotted the IR spectra of typical ices with a UV fluence of $1.0 \times 10^{18}$ photons cm$^{-2}$ in the range of 900−2300 cm$^{-1}$, and presented them in Fig. 2. In this figure, the ice mixtures are shown in upper panel: (A) 50 ML, 14 K, $CD_4$:$O_2$ = 1:1 mixed ices; (B) 80 ML, 14 K, $CH_4$:$O_2$ = 1:1 mixed ices; (C) 80 ML, 14 K, $CH_4$:$CD_4$:$O_2$ = 1:1:2 mixed ices; the pure ices are shown in lower panel: (D) 60 ML, 14 K, $O_2$ ice; (E) 80 ML, 14 K, $CH_4$ ice; (F) 40 ML, 14 K, $CD_4$ ice. The positions of IR bands for reactants and products are represented by the grey dashed lines and names. The spectral bands used for quantification are represented by a rectangular grey area.

Moreover, the chemical composition of these ices has been identified and clearly labelled in Fig. 2. Clearly, the composition of these ice samples changed after UV irradiation. Therefore, each ice sample is illustrated in detail, and we will analyse the dissociation pathways of pure and mixed ices in the next subsection. The following subsections focus on: (3.1) pure $CH_4$ ice; (3.2) pure $O_2$ ice; and (3.3) $CH_4$:$O_2$ ice mixtures, respectively.

**Table 1.** List of ice samples. In addition, the quantification analysis data, such as the photoproduction rates of $CH_2O$, $CH_3OH$, CO, $H_2O$ ($10^{-18}$ cm$^{-2}$/$N_{CH4}$(0)), and $O_3$ ($10^{16}$ photon$^{-1}$ ML$^{-1}$) as well as the photodestruction cross-sections of $CH_4$ and $CD_4$ ($10^{-19}$ cm$^{-2}$), is also presented after an UV fluence of $1.0 \times 10^{18}$ photons cm$^{-2}$. Different units for the formation rates of $O_3$ and other products are used due to different calculation methods.

| No. | Ices | Ratio | Temp. (K) | Thick. (ML)[a] | $CH_2O$[b] | $CH_3OH$[b] | CO[b] | $H_2O$[b] | $O_3$ [b] | Cross-sections[b] |
|---|---|---|---|---|---|---|---|---|---|---|
| 1 | $O_2$ | – | 14 | 60 | – | – | – | – | 18(1.0) | – |
| 2 | $CH_4$ | – | 14 | 80 | – | – | – | – | – | 0.7(0.1) |
| 3 | $CD_4$ | – | 14 | 40 | – | – | – | – | – | 0.8(0.1) |
| 4 | $CH_4$:$O_2$ | 1:1 | 20 | 80 | 1.5(0.2) | 0.8(0.1) | 2.7(0.1) | 8(2.0) | 5.4(1.4) | 0.8(0.1) |
| 5 | $CH_4$:$O_2$ | 1:1 | 17 | 40 | 2.8(0.2) | 1.5(0.1) | 4.9(0.1) | 18(1.0) | 3.7(1.4) | 1.6(0.1) |
| 6 | $CH_4$:$O_2$ | 1:1 | 14 | 8 | 5.5(0.8) | 1.8(0.1) | 4.5(0.7) | 42(2.0) | – | 2.8(0.2) |
| 7 | $CH_4$:$O_2$ | 1:1 | 14 | 40 | 4.1(0.3) | 1.8(0.1) | 5.6(0.1) | 20(1.0) | 3.8(1.6) | 2.1(0.1) |
| 8 | $CH_4$:$O_2$ | 1:1 | 14 | 80 | 4.7(0.2) | 1.8(0.1) | 4.4(0.1) | 15(1.0) | 5.1(1.4) | 1.6(0.1) |
| 9 | $CH_4$:$O_2$ | 1:3 | 14 | 60 | 5.1(0.3) | 1.6(0.1) | 6.3(0.2) | 18(1.0) | 9.8(1.1) | 3.3(0.1) |
| 10 | $CH_4$:$O_2$ | 3:1 | 14 | 100 | 3.0(0.1) | 1.3(0.1) | 3.1(0.1) | 9(1.0) | 4.1(2.4) | 0.8(0.1) |
| 11 | $CD_4$:$O_2$ | 1:1 | 14 | 50 | 3.4(0.1) | 1.5(0.1) | – | 9(1.0) | 4.3(0.5) | 2.4(0.1) |
| 12 | $CH_4$:$CD_4$:$O_2$ | 1:1:2 | 14 | 80 | – | – | – | – | – | 1.7(0.1)($CH_4$/$CD_4$) |

*Notes*. [a]1 ML = $10^{15}$ molecules cm$^{-2}$.
[b]After an UV fluence of $1.0 \times 10^{18}$ photons cm$^{-2}$. The values in parentheses represent the uncertainties, which are estimated to be of the order of 10 per cent.

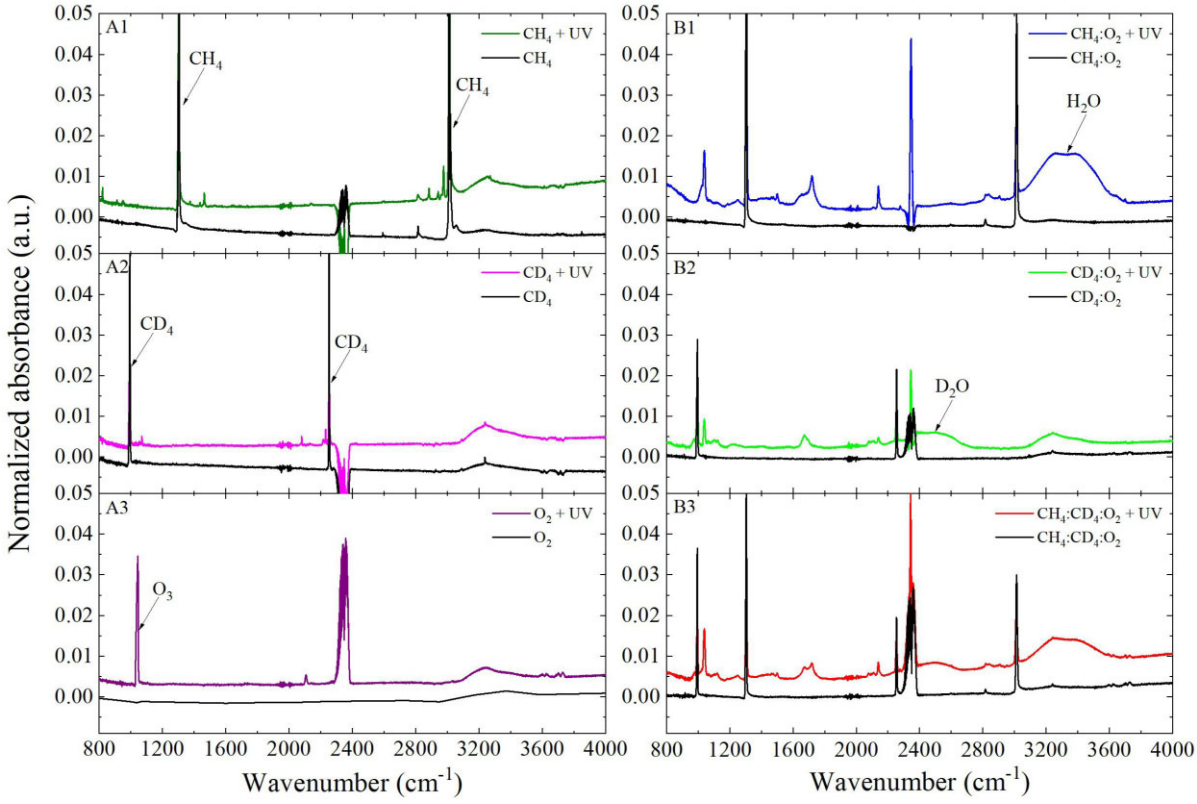


**Figure 1.** Overall IR spectra of pure ices (left panels) and mixed ices (right panels) before and after UV irradiation at the range of 800−4000 cm$^{-1}$. The total UV fluence is $1.0 \times 10^{18}$ photons cm$^{-2}$ for irradiated 3 h. Left panels: (A1) 80 ML, 14 K, $CH_4$ ice; (A2) 40 ML, 14 K, $CD_4$ ice; (A3) 60 ML, 14 K, $O_2$ ice; right panels: (B1) 80 ML, 14 K, $CH_4$:$O_2$ = 1:1 mixed ices; (B2) 50 ML, 14 K, $CD_4$:$O_2$ = 1:1 mixed ices; (B3) 80 ML, 14 K, $CH_4$:$CD_4$:$O_2$ = 1:1:2 mixed ices. The coloured lines represent ice samples exposed to UV irradiation, while the black lines represent the ice without UV irradiation.

### 3.1 Pure $CH_4$ ice

As we can see in Fig. 2(E), new products (i.e. $C_2H_6$, $C_3H_8$, and $C_2H_4$) are identified in pure irradiated $CH_4$ ice (Öberg et al. 2008). Fig. 3 presents IR spectra of pure $CH_4$ (80 ML, 14 K) ice as a function of UV irradiation time. The total UV fluence is $1.0 \times 10^{18}$ photons cm$^{-2}$ for irradiated 3 h. The inset zoom-in IR spectra in Figs 3 (A) and 3 (B) reveal more details of the photoproducts (i.e. $C_2H_4$, $C_2H_6$, and $C_3H_8$). With increasing UV fluence, the absorbance of the $CH_4$ band (3010 cm$^{-1}$) gradually decreases, while the absorbance of $C_2H_4$ band (1436 cm$^{-1}$), $C_2H_6$ band (2941 and 2975 cm$^{-1}$), and $C_3H_8$ band (2959 cm$^{-1}$) gradually increases.

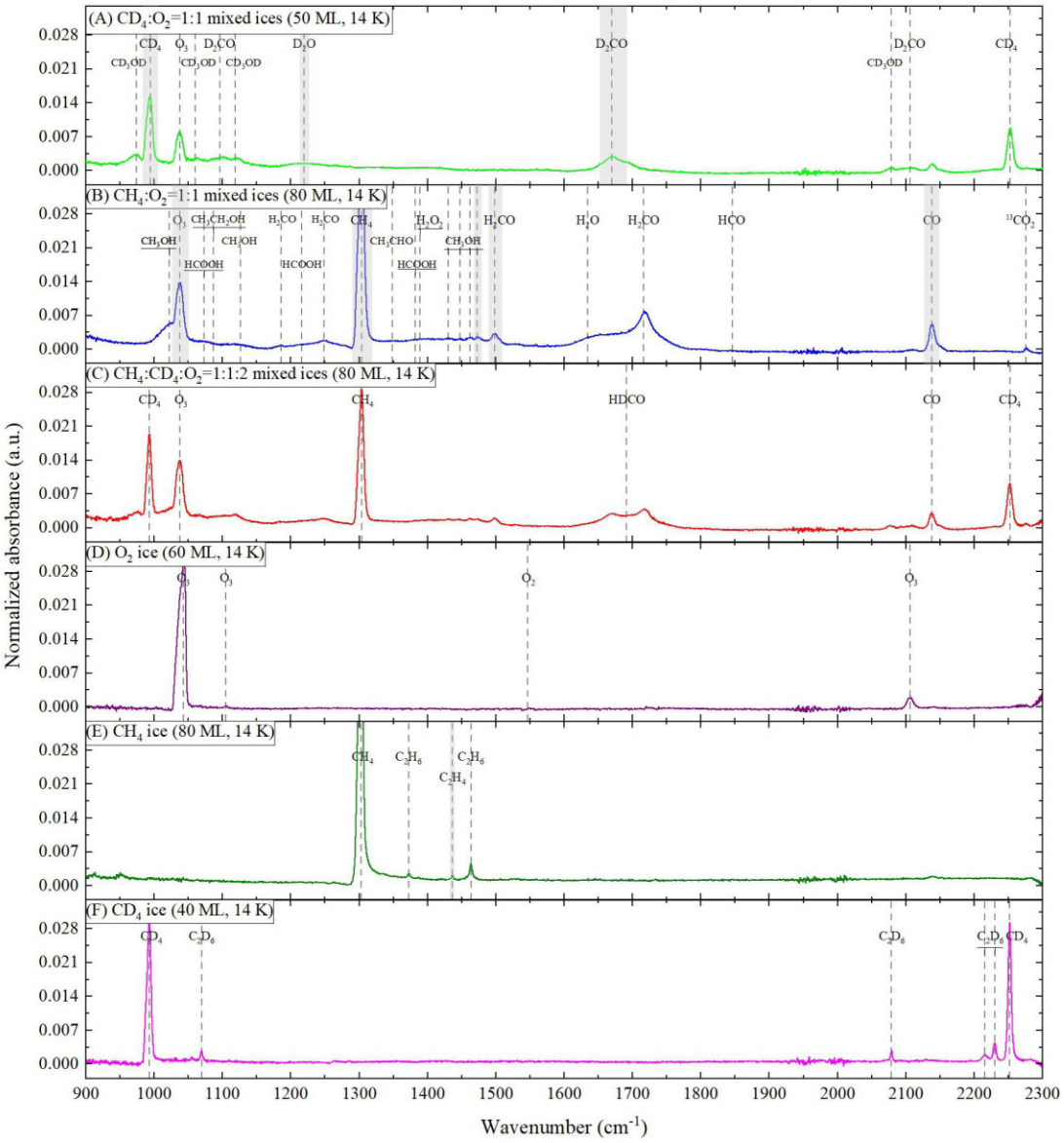


**Figure 2.** IR spectra of irradiated ices with an UV fluence of $1.0\times10^{18}$ photons $cm^{-2}$ at the range of 900−2300 $cm^{-1}$: (A) 50 ML, 14 K, $CD_4$:$O_2$ = 1:1 mixed ices; (B) 80 ML, 14 K, $CH_4$:$O_2$ = 1:1 mixed ices; (C) 80 ML, 14 K, $CH_4$:$CD_4$:$O_2$ = 1:1:2 mixed ices; (D) 60 ML, 14 K, $O_2$ ice; (E) 80 ML, 14 K, $CH_4$ ice; (F) 40 ML, 14 K, $CD_4$ ice. The positions of IR bands for reactants and products are represented by the grey dash and names. The spectral bands used for quantification are represented by the grey rectangular area: in pure $CH_4$ ice, the $CH_4$ bands at 1300 and 3010 $cm^{-1}$ was used to track destruction, while some spectral bands such as $C_2H_6$ bands at 2975 $cm^{-1}$ and 2941 $cm^{-1}$, $C_2H_4$ band at 1436 $cm^{-1}$ and $C_3H_8$ band at 2959 $cm^{-1}$ were used to track formation. In the mixed ices, the $CH_4$ bands at 1300 and 3010 $cm^{-1}$ and $CD_4$ band at 1039 $cm^{-1}$ were used to track destruction, while some spectral bands such as $H_2O$ band at 3280 $cm^{-1}$, $CH_3OH$ band at 1474 $cm^{-1}$, $CH_2O$ band at 1500 $cm^{-1}$, $O_3$ band at 2105 $cm^{-1}$, CO band at 2139 $cm^{-1}$, $D_2O$ band at 1210 $cm^{-1}$, and $CD_2O$ band at 1670 $cm^{-1}$, were used to track formation.

For pure irradiated $CD_4$ ice, only $C_2D_6$ is formed in Fig. 2(F), and no band feature can be labelled as $C_2D_4$ and other D-products (e.g. $C_3D_8$) (Shimanouchi 1972). This may be influenced by the isotope effects, meaning that the mass difference between isotope atoms (i.e. H and D atoms) affects the reaction rate of radicals involved in these isotope atoms and thus affects the formation of photoproducts. In other words, during the dissociation process of pure $CD_4$ ice, the rate at which the chemical bonds involved in the breakage of the D atom will be reduced due to the high mass of the D atom compared to the H atom, resulting in the inhibition of D-products (e.g. $C_2D_4$ and $C_3D_8$) formation.

### 3.2 Pure $O_2$ ice

As shown in Fig. 1(A3), before UV irradiation, $O_2$ without infrared activity cannot be detected. Furthermore, as the photoproduct of the $O_2$ ice, $O_3$ (1037 $cm^{-1}$) could be identified in Fig. 2(D). The photochemistry of pure $O_2$ ice has been studied (Zhen & Linnartz 2014). In pure $O_2$ ice, $O_2$ can be photodissociated into energetic O atoms, then they will form $O_3$ or recombine to $O_2$. The $O_3$ produced on the irradiated $O_2$ ice can still be photodissociated into the energetic O atom and $O_2$, or form complexes such as $O_3\cdots O$ and $[O_3]_n$ by reacting with the surrounding O and $O_3$, respectively. The ozone

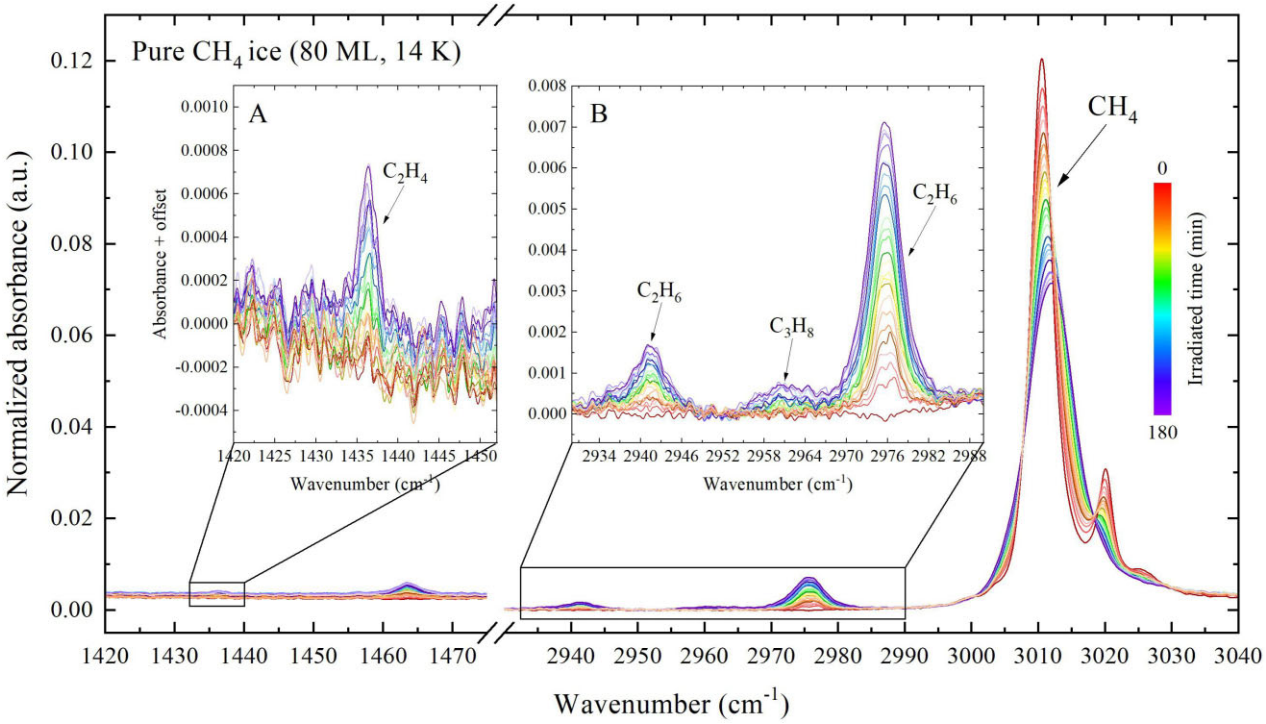


**Figure 3.** IR spectra of pure $CH_4$ ice (80 ML, 14 K) as a function of UV irradiated time. The total UV fluence is $1.0 \times 10^{18}$ photons $cm^{-2}$ for irradiated 3 h. The inset zoom-in IR spectra reveal more details of the photoproducts (i.e. $C_2H_4$, $C_2H_6$, and $C_3H_8$).

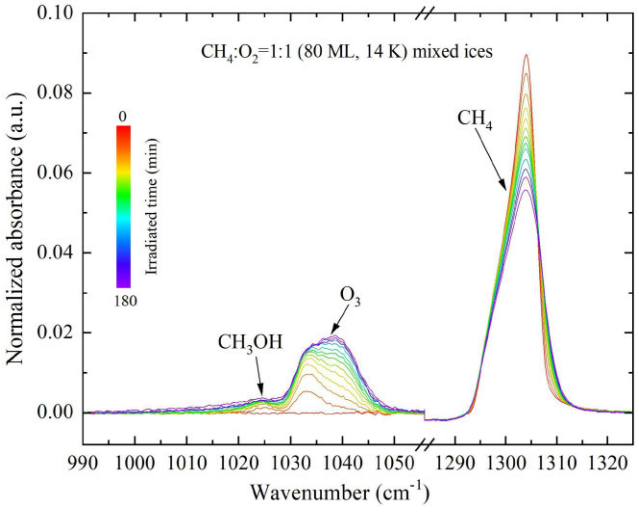


**Figure 4.** IR spectra of $CH_4$, $O_3$, and $CH_3OH$ in the $CH_4$:$O_2$ = 1:1 (80 ML, 14 K) mixed ices as a function of UV irradiated time. The total UV fluence is $1.0 \times 10^{18}$ photons $cm^{-2}$ for irradiated 3 h.

monomer at 1037 $cm^{-1}$ and two close satellite peaks at 1032 and 1042 $cm^{-1}$ could be seen in Fig. 4. For two satellite peaks, the former is attributable to the ozone-oxygen complex ($O_3 \cdots O$); the latter can be assigned to the ozone dimer ($O_3 \cdots O_3$) and ozone cluster (Zhen & Linnartz 2014).

### 3.3 $CH_4$:$O_2$ ice mixtures

Before irradiation, the IR spectra of mixed ices are similar to those of pure ices, except around 1550 $cm^{-1}$, which is a small peak assigned to the O-O stretching for $\nu_1$ fundamental mode of $O_2$ (Freiman & Jodl 2004). In mixed ices, the local interactions with polar species or matrix-induced asymmetry can induce a transient dipole moment, making the $O_2$ stretch weakly IR-active. However, this effect for the transient dipole moment is not guaranteed, so the 1550 $cm^{-1}$ peak may be absent in some ice mixtures, and its reason remains unclear. Upon irradiation, a series of new species are effectively formed. In addition, the absorption characteristics of these species are identified throughout the spectra and are listed in Table 2. In addition, we note that in Fig. 1, the spectra profile without and with UV irradiation reveals an absorption feature of gas-phase $CO_2$. This occurs because our FTIR system operates under conditions that are not fully vacuum purged, so the MCT detector is continuously purged with dry air. In addition, the IR spectra presented represent the difference spectra by subtracting the initial background spectrum from the sample spectrum (signal + background). Due to a minor temporal drift in the background signal during experiments, a residual gas-phase $CO_2$ cannot be completely eliminated despite background subtraction.

With respect to irradiated $CH_4$:$O_2$ ice mixtures, we only focus on the 'region of interest' in the vicinity of 900–2300 $cm^{-1}$, as shown in Fig. 2(A–C). The molecular species associated with this region have been identified and labelled. In addition, the spectra of pure irradiated ices of $O_2$, $CH_4$, and $CD_4$ have been included in Fig. 2(D–F) for comparison with mixed irradiated ices. In Fig. 2(B), most of the spectral features that appear upon irradiation can be assigned to these molecules: $CH_2O$, $CH_3OH$, $O_3$, CO, $CO_2$, $H_2O$, $H_2O_2$, HCOOH, $CH_3CH_2OH$, and $CH_3CHO$. Furthermore, we also identified the band feature of the HCO radical around 1842 $cm^{-1}$.

Fig. 4 presents IR spectra of $CH_4$:$O_2$ = 1:1 (80 ML, 14 K) mixed ices as a function of UV irradiated time in the range of 990–1325 $cm^{-1}$. In this figure, the change of $CH_4$, $O_3$, and $CH_3OH$ could be observed in detail. As the irradiation time is longer, the

**Table 2.** IR spectral features and band strengths of ices.

| Species | Assignment | Band | Band Strength |
|---|---|---|---|
| | | $cm^{-1}$ | $10^{-18}$ cm molecule$^{-1}$ |
| $CH_4$ | CH deformation | 1300 | 6.1 |
| | CH stretch | 3010 | 6.4 |
| $CD_4$ | CD deformation | 1039 | 3.0 |
| | CD stretch | 2254 | 3.6 |
| $C_2D_6$ | $\nu_8$ ($e_\mu$) | 1070 | – |
| | $a_{2\mu}$ | 2080 | – |
| $C_3H_8$ | $CH_3$ symmetric stretch | 2962 | 15.8 |
| $C_2H_6$[,,] | $\nu_8$ ($e_\mu$) | 1464 | 4.5 |
| | $CH_3$ symmetric stretch | 2942 | 3.5 |
| | $CH_3$ degenerate stretch | 2976 | 10.5 |
| $C_2H_4$ | $CH_2$ deformation | 1436 | 2.9 |
| $^{13}CO_2$ | $^{13}CO$ stretch | 2276 | 78 |
| $H_2O$ | OH stretch | 3280 | 200 |
| | OH bend | 1670 | 12 |
| $CH_2O$[,] | $CH_2$ scissoring | 1500 | 3.9 |
| | CO stretching | 1720 | 1.83 |
| $CH_3OH$[,,] | $CH_3$ deformation | 1474 | [a]4.5 |
| | CO stretching | 1026 | [a]18 |
| HCOOH | OH bend | 1223 | [a]15 |
| $C_2H_5OH$[,] | | 1044 | [a]19 |
| $CH_3CHO$[,] | $CH_3$ s-deform | 1350 | [a]4.5 |
| CO | $^{12}CO$ stretch | 2139 | 11 |
| $O_3$ | Combination | 2105 | 1.3 |
| | OO asymmetric stretch | 1037 | 15 |
| HCO | CO stretch | 1842 | – |
| HDCO | CO stretching | 1694 | – |
| $D_2O$ | OD bend | 1210 | 6.0 |
| | OD stretch | 2484 | 140 |
| $D_2CO$ | $CD_2$ scissoring | 1101 | 5.3 |
| | CO stretching | 1670 | 13 |
| $CD_3OD$ | CO stretching | 974 | – |
| | $CD_3$ asymmetry bend | 1063 | – |
| | $CD_3$ symmetry bend | 1120 | – |

*Notes*. [a]In an $H_2O$ ice matrix. [b]Moore & Hudson (1998). [c]Shimanouchi (1972). [d]Gerakines et al. (1995). [e]Schutte, Allamandola & Sandford (1993). [f]Kerkhof, Schutte & Ehrenfreund (1999). [g]Brewer & Wang (1972). [h]Hidaka et al. (2009). [i]Bennett et al. (2005). [j]Bennett et al. (2006). [k]Bennett et al. (2007). [l]de Barros et al. (2011). [m]de Barros et al. (2014). [n]The spectral features used for quantification analysis. [o]The band strengths with an uncertainty of ∼20 per cent–30 per cent.

band absorbance of the reactant $CH_4$ gradually decreases, while photoproducts such as $CH_3OH$ and $O_3$ are formed, and their band absorbance gradually increases. Interestingly, the ozone dimer ($O_3 \cdots O_3$) are also observed around 1042 $cm^{-1}$.

Upon UV irradiation, most $CH_4$:$O_2$ mixtures – regardless of the mixing ratio or temperature – produced similar products. However, some species with the least abundance are not detected under some experimental conditions. In addition, Figs 2 (A) and (C) show the IR spectra of irradiated $CD_4$:$O_2$ = 1:1 and $CH_4$:$CD_4$:$O_2$ = 1:1:2 mixed ices, and the following D products, such as $CD_3OD$, HDCO, $D_2O$, and $CD_2O$, are identified. For the identification of mid-IR absorption bands, isotopic labelling helps constrain the candidates for some absorption bands.

## 4 QUANTIFICATION ANALYSIS

As in the experiment results presented above, the photochemistry processes of the ices lead to complex photoproducts according to the radical–radical and radical-atom/molecule reaction schemes (Öberg et al. 2009a, b). In order to better understand their photoevolution mechanism, we have processed and analysed these experimental data further. In the following quantitative analysis, we only consider the dissociation and recombination of first-generation radicals from $CH_4$ and $O_2$ photodissociation and study the formation processes of $O_3$, $H_2O$, and $CH_3OH$. The following subsections focus on: (4.1) the photodestruction cross-sections of $CH_4$ and $CD_4$; (4.2) the quantification of $O_3$ formation; and (4.3) the quantification of $H_2O$ and $CH_3OH$ formation, respectively.

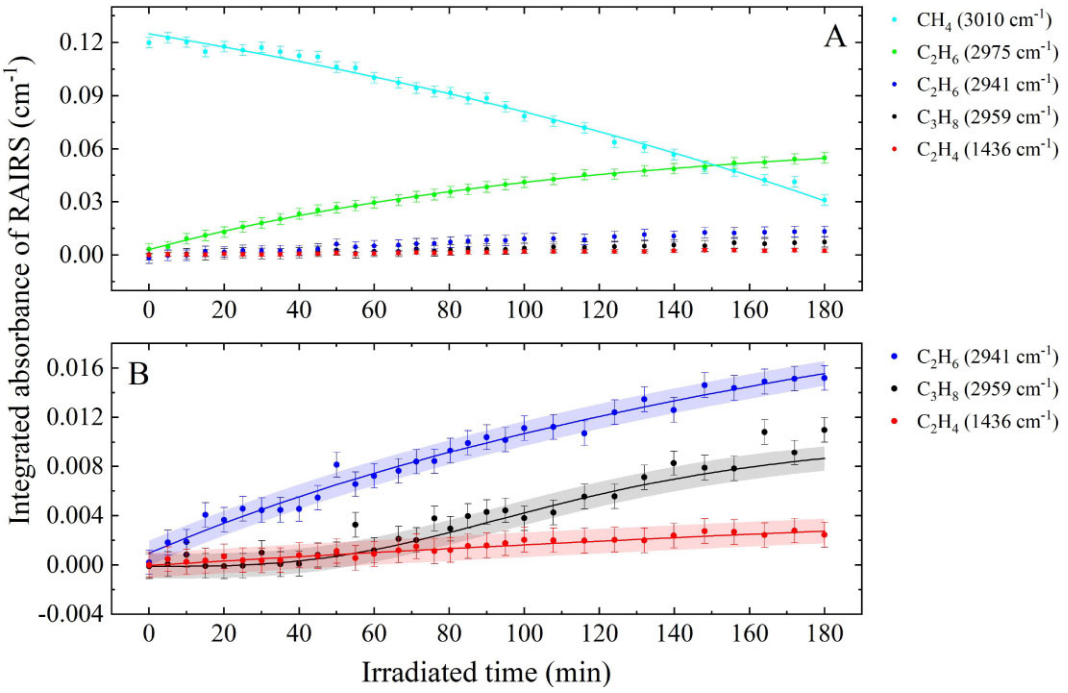


**Figure 5.** Quantified production of products in pure $CH_4$ ice (80 ML, 14 K) as a function of UV irradiated time. The total UV fluence is $1.0 \times 10^{18}$ photons cm$^{-2}$ for irradiated 3 h. Panel (A): The integrated RAIRS absorbance for $CH_4$, $C_2H_4$, $C_2H_6$, and $C_3H_8$; Panel (B): The inset zoom-in scatter plots and fitting lines of $C_3H_8$, $C_2H_4$, and $C_2H_6$ (2941 cm$^{-1}$). In addition, the error bars of fitting lines in panel (B) are shown by a coloured rectangular area.

### 4.1 The photodestruction cross-sections of $CH_4$ and $CD_4$

The photodestruction rate of a species, averaged over the UV spectrum, is determined by the amount of available radicals for diffusion and subsequent reactions. It can be calculated from the measured loss of the intensity of the $CH_4$ and $CD_4$ bands with UV fluence on pure or mixed ices. These band positions and their strengths used for the quantification analysis are labelled with stars in Table 2. The band strengths have an uncertainty of ∼20 per cent–30 per cent due to different references, ice compositions, and/or ice temperatures, but we assume that it does not affect the ice quantification analysis. The same band strengths are selected for each molecule for all different experimental conditions.

As shown in Fig. 5, quantified production of products is presented for pure irradiated $CH_4$ ice (80 ML, 14 K). In this figure, panel (A) shows the integrated RAIRS absorbance of $CH_4$ (3010 cm$^{-1}$), $C_2H_6$ (2975 cm$^{-1}$, 2941 cm$^{-1}$), $C_3H_8$ (2959 cm$^{-1}$), and $C_2H_4$ (1436 cm$^{-1}$); panel (B) shows the inset zoom-in scatter plots and fitting lines of $C_3H_8$, $C_2H_4$, and $C_2H_6$ (2941 cm$^{-1}$) in panel (A).

As shown in Fig. 5 (A), the $CH_4$ absorbance exhibits a monotonic decrease with increasing irradiation time, mainly due to the photofragmentation processes of $CH_4$. The photofragmentation processes of $CH_4$ mainly depend on the flux of UV photons. According to that, the $CH_4$ absorbance decreases as an exponential function of the irradiation time.

As the UV irradiation time increases, the integrated RAIRS absorbance of $C_2H_6$ (2975 cm$^{-1}$), $C_3H_8$ (2959 cm$^{-1}$), $C_2H_6$ (2941 cm$^{-1}$), and $C_2H_4$ (1436 cm$^{-1}$) gradually increases. In Fig. 5(B), we can clearly find that the integrated RAIRS absorbance of $C_3H_8$ increases slowly compared to $C_2H_4$ and $C_2H_6$ at the beginning of irradiation, but its integrated RAIRS absorbance increases rapidly after ∼1 h of UV irradiation, which suggests that $C_2H_6$ and $C_2H_4$ are the second generation products that directly formed through the recombination of the photofragments of $CH_4$, and $C_3H_8$ is the third generation product that formed from the photofragments of $C_2H_6$ and $CH_4$. In addition, the reaction scheme will be discussed in the next section.

Furthermore, we assume that the $CH_4$ destruction rate does not change throughout the irradiation period. However, the $CH_4$ destruction rate will be affected by other effects, such as the shelf-shielding effect. The newly formed species (e.g. $C_2H_6$ and $C_2H_4$) will prohibit UV penetration in the ice or at least limit its impact to the top layers only. In addition, as catalogued in Fig. 5, the primary photoproducts were identified spectroscopically. However, some secondary photoproducts were not detected by FTIR spectroscopy because of insufficient absorption cross-sections or spectral overlap. As a result, the formation rate of some primary products (e.g. $C_2H_4$ and $C_2H_6$) exhibited no significant increase over the experimental time-scale.

Fig. 6 shows the quantitative loss of $CH_4$ and $CD_4$ in the ice mixtures during UV irradiation and plots their normalized and logarithmically transformed loss as a function of the fluence of UV under different conditions. The results on the photodestruction cross-sections of $CH_4$ and $CD_4$ are listed in Table 1, and the uncertainties are estimated to be of the order of 10 per cent. The photodestruction cross-section of pure $CH_4$ ice is consistent with the previous report (Cottin, Moore & Bénilan 2003), and roughly in agreement with the estimate by Öberg et al. (2008). We only fitted the first part of the curves when they were still approximately linear, and the error may come from the fitting procedures. As shown in Fig. 6, the linear logarithmic transformation loss plot is obtained as a result of the exponential decay of $CH_4$ depletion.

According to the values obtained presented in Table 1 and Fig. 6, we can have: first, the photodestruction cross-sections of $CH_4$ decrease as the thicknesses of the mixed ices increase, for example, 2.8 ± 0.2 ($N_6$, 8 ML), 2.1 ± 0.1 ($N_7$, 40 ML), and 1.6 ± 0.1 ($N_8$,

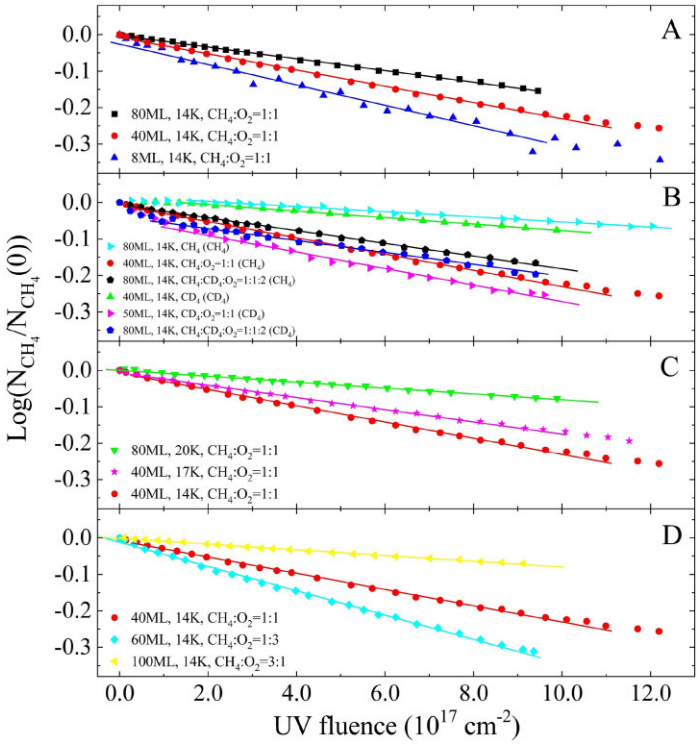


**Figure 6.** Normalized and log-transformed loss of $CH_4$. (A) Different thicknesses; (B) Pure and mixed ices; (C) Different temperatures; and (D) Different mixed ratios.

80 ML). The observed attenuation in photodestruction efficiency arises from four distinct mechanisms: (i) radiation attenuation via Beer–Lambert law decay; (ii) competitive absorption by accumulated photoproducts; (iii) diffusion-limited radical recombination enhancing backward reactions; and (iv) phase-transition-induced immobilization of reactants in crystalline lattices; second, within the experimental uncertainties, the isotope D compared to H has a minor effect on the photodestruction cross-section, e.g. for pure ices, 0.7 ± 0.1 ($N_2$, $CH_4$) and 0.8 ± 0.1 ($N_3$, $CD_4$), while for mixed ices, 2.1 ± 0.1 ($N_7$, $CH_4$), 2.4 ± 0.1 ($N_{11}$, $CD_4$), and 1.7 ± 0.1 ($N_{12}$, $CH_4/CD_4$);

Third, photodestruction cross-sections gradually decrease with increasing temperature, for example, 2.1 ± 0.1 ($N_7$, 14 K), 1.6 ± 0.1 ($N_5$, 17 K), and 0.8 ± 0.1 ($N_4$, 20 K), which indicates that there is no significant recombination reaction at low temperatures. This is consistent with the higher gas-phase $CH_4$ UV-absorption cross-section that the recombination can be ignored in the gas phase; fourth, the photodestruction cross-sections increase as the mixed ratio of $CH_4$:$O_2$ decreases, e.g. 0.8 ± 0.1 ($N_{10}$, $CH_4$:$O_2$ = 3:1), 2.1 ± 0.1 ($N_7$, $CH_4$:$O_2$ = 1:1), and 3.3 ± 0.1 ($N_9$, $CH_4$:$O_2$ = 1:3), which is due to the higher density of reactive O-related species formed on the gold surface; fifth, through comparing the photodestruction cross-sections in pure and mixed ices, it is obvious that more $CH_4/CD_4$ are destroyed in mixed ices than in pure ices during irradiation, e.g. 0.7 ± 0.1 ($N_2$, $CH_4$), 2.1 ± 0.1 ($N_7$, $CH_4$).

### 4.2 The quantification of $O_3$ formation

In pure $O_2$ ice or other $O_2$-containing ices, $O_3$ is formed immediately upon UV irradiation, and the transformation between $O_2$ and $O_3$ reaches an equilibrium rapidly. As shown in Fig. 4, for the ice mixture $CH_4$:$O_2$ = 1:1 (80 ML, 14 K), the band absorbance intensity of $O_3$ gradually increases as a function of irradiation time. Soon after

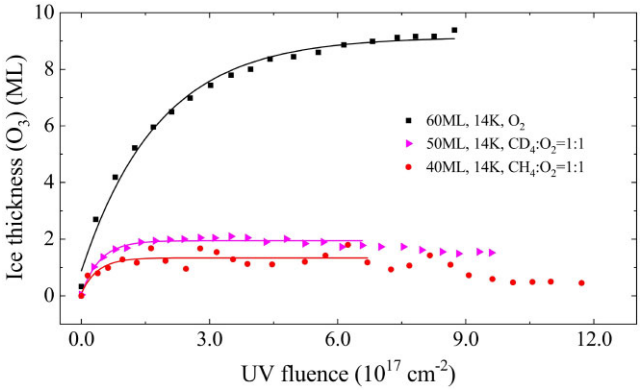


**Figure 7.** The temporal thickness growth of ozone ($O_3$, 2105 $cm^{-1}$) as a function of UV fluence.

irradiation started, the top layer of the ices, such as $CH_4$, $O_2$, and $O_3$, would be destroyed and transformed into other species. In Fig. 7, we have obtained the growth in temporal thickness of $O_3$ in pure $O_2$ ice, $CH_4$:$O_2$, and $CD_4$:$O_2$ mixed ices. Obviously, the thickness of the $O_3$ ice in pure $O_2$ ice increases at a higher rate in comparison with $O_2$-containing mixed ices, which is because oxygen atoms in the mixed ices will still react with other radicals or molecules such as H and $CH_3$.

In addition, Table 1 lists the formation rates of $O_3$ on different ices. We can clearly see that its formation rates in the mixed ices are significantly lower than in pure $O_2$ ice, e.g. 18 ± 1.0 ($N_1$, $O_2$) and 3.8 ± 1.6 ($N_7$, $CH_4$:$O_2$ = 1:1). The photoproduction rates of $O_3$ increase as the ratio of $O_2$ in the $CH_4$:$O_2$ mixed ices increases, e.g. 4.1 ± 2.4 ($N_{10}$, $CH_4$:$O_2$ = 3:1), 5.1 ± 1.4 ($N_8$, $CH_4$:$O_2$ = 1:1), and 9.8 ± 1.1 ($N_9$, $CH_4$:$O_2$ = 1:3). The decline in $O_3$ is rather slower, which means

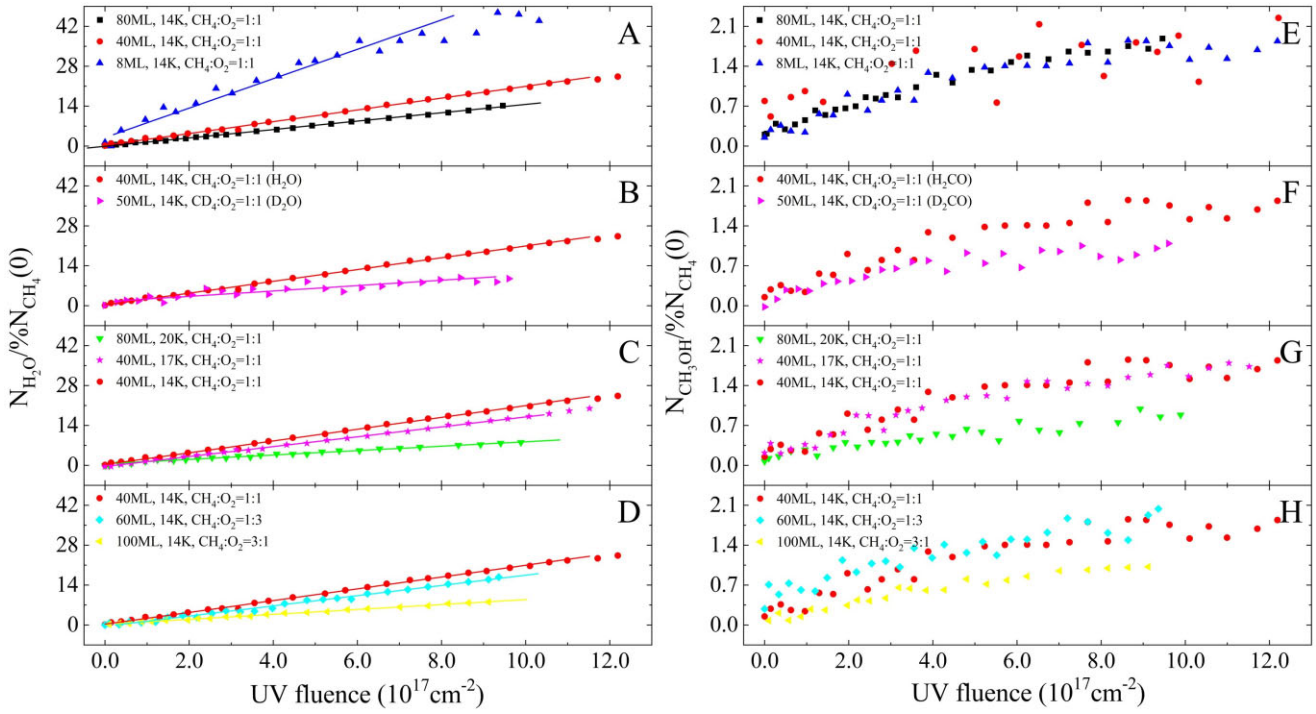


**Figure 8.** Quantified production of $H_2O$ and $CH_3OH$ under different conditions as a function of UV fluence.

that the concentration of O-related radicals remains constant, as they are intermediates in the formation network of $H_2O$ and/or organic molecules.

### 4.3 The quantification of $H_2O$ and $CH_3OH$ formation

In mixed ices, the dissociation pathways of $CH_4$ and $CD_4$ are similar to those in pure ices. However, the reaction network in the mixed ices is complex and diverse, and most reactions take place between $CH_4$-related species (H and $CH_3$) and $O_2$-related species (O, $O_2$, and $O_3$). Surprisingly, there is no band characteristic that can be assigned to $C_2H_6$ and $C_2H_4$ in the ice mixtures. In the irradiated mixed ices, two of the most representative products are $H_2O$ and $CH_3OH$, and below, we will discuss their production methods under different experimental conditions. Fig. 8 shows the quantified production of $H_2O$ and $CH_3OH$ as a function of UV fluence. In addition, the obtained photoproduction rates are listed in Table 1, and the uncertainties are estimated to be of the order of 10 per cent.

#### *4.3.1 The quantification of $H_2O$ formation*

In the case of $H_2$ O, from the values obtained in Table 1 and Fig. 8(A–D), we can find: First, the photoproduction rate of $H_2O$ increases when the thickness of mixed ices decreases, e.g. 15 ± 1.0 ($N_8$, 80 ML), 20 ± 1.0 ($N_7$, 40 ML), and 42 ± 1.0 ($N_6$, 8 ML), which suggests the reactions not only take place in the top layers; Second, taking the isotope effect into account, the photoproduction rate of water is significantly different, e.g. 20 ± 1.0 ($N_7$, $H_2O$) and 9 ± 1.0 ($N_{11}$, $D_2O$). Since there is no diffusion barrier for H and D, these differences are mainly due to different behaviours of intermediate species (that is, OH, $HO_2$, OD, and $DO_2$) in the formation pathways of $H_2O$ and $D_2O$ (Ioppolo et al. 2008).

Third, the photoproduction rate increases with decreasing temperature, e.g. 8 ± 2.0 ($N_4$, 20 K), 18 ± 1.0 ($N_5$, 17 K), and 20 ± 1.0 ($N_7$, 14 K), meaning negative correlation between the photoproduction rate of $H_2O$ and temperature. The main production pathway of $H_2O$ is the reaction between OH and H, so the quantity and diffusion rates of H and OH greatly affect the production of $H_2O$. Furthermore, their diffusion rates are mainly affected by the temperature of the ice, but in the range of 14–21 K, the diffusion rates of the H and OH radicals could be treated as the same. When the ice temperature decreases, on the one hand, more radicals can be trapped in the ice, but the recombination rate between radicals decreases due to reduced reactivity; on the other hand, the number of radicals increases so that the chance of collision of OH with H becomes higher. As a result, in general, the photoproduction rate of $H_2O$ is higher at a lower temperature.

Fourth, the photoproduction rate gradually decreases with increasing ratios of $CH_4$:$O_2$ mixed ices, for example, 18 ± 1.0 ($N_9$, $CH_4$:$O_2$ = 1:3), 20 ± 1.0 ($N_7$, $CH_4$:$O_2$ = 1:1), and 9 ± 1.0 ($N_{10}$, $CH_4$:$O_2$ = 3:1). As shown in Fig. 9, the photoproduction rates of $H_2O$ and $CH_3OH$ under different mixed ratios are presented. Among the above three mixed ratios, $CH_4$:$O_2$ = 1:1 is the most productive ratio for $H_2O$. One possible reason is the lower density of O atoms affecting the quantity of OH radicals in the ice ratio of $CH_4$:$O_2$ = 3:1 and the lower density of H radicals in the ice ratio of $CH_4$:$O_2$ = 1:3.

#### *4.3.2 The quantification of $CH_3OH$ formation*

As shown in Fig. 4, $CH_3OH$, as one of the representative organic compounds, has a band absorbance intensity that increases rapidly in the beginning and soon reaches equilibrium. Fig. 8(E–H) shows the quantified production of $CH_3OH$ in the different ice mixtures as a function of UV fluence. The mechanism of $CH_3OH$ production is mainly the reaction of $CH_3$ with OH radicals, which is similar to the formation pathway of $H_2O$. However, for $CH_3OH$ or other organic compounds, their formation reactions are in a chain reaction, so these compounds will continue to be photodissociated upon UV

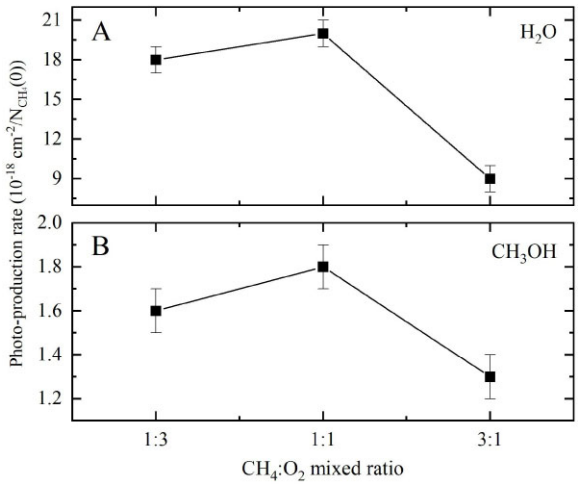


**Figure 9.** The photoproduction rates of $H_2O$ and $CH_3OH$ after an UV fluence of $1.0 \times 10^{18}$ photons cm$^{-2}$ under different mixed ratios of $CH_4$:$O_2$ ices (14 K).

irradiation and form more complex organic compounds through the recombination of radicals.

According to the values obtained shown in Table 1 and Fig. 8(E–H), we can find: first, for the photoproduction rate, the thickness dependence is not observed, e.g. 1.8 ± 0.1 ($N_8$, 80 ML), 1.8 ± 0.1 ($N_7$, 40 ML), and 1.8±0.1 ($N_6$, 8 ML). Therefore, it applies to the top layers reaction model, indicating that the diffuse rate of $CH_3$ radicals is higher; second, given the isotope effect, there is no significant difference, e.g. 1.8 ± 0.1 ($N_7$, $CH_3OH$) and 1.5 ± 0.1 ($N_{11}$, $CD_3OD$), meaning that the diffusion rates of H-radical (i.e. $CH_3$ and OH) and D-radical (i.e. $CD_3$ and OD) are similar; Third, the photoproduction rate decreases with increasing temperature, e.g. 1.8 ± 0.1 ($N_7$, 14 K), 1.5 ± 0.1 ($N_5$, 17 K), and 0.8 ± 0.1 ($N_4$, 20 K). In other words, like $H_2O$, the photoproduction rate of $CH_3OH$ has a negative temperature dependence effect; fourth, the photoproduction rate is also affected by the ratio of mixed ices, e.g. 1.6 ± 0.1 ($N_9$, $CH_4$:$O_2$ = 1:3), 1.8 ± 0.1 ($N_7$, $CH_4$:$O_2$ = 1:1), and 1.3 ± 0.1 ($N_{10}$, $CH_4$:$O_2$ = 3:1). As shown in Fig. 9(B), $CH_3OH$ is the most abundant in the $CH_4$:$O_2$ = 1:1 mixed ices, which maybe because both $CH_3$ and the OH radicals have a higher density. In addition, the quantity of $CH_3$ and OH radicals depends on the photodissociation efficiency of $CH_4$ and $O_2$, respectively.

## 5 DISCUSSION

Fig. 10 presents the reaction scheme of pure $CH_4$ and $CH_4$:$O_2$ ice processing after UV irradiation in this work. The red and black words with solid boxes represent reactants and products, respectively, while the grey words with dotted boxes represent radicals. The UV denotes UV irradiation or UV irradiation analogues. Moreover, the reaction energies have been calculated for all pathways in Fig. 10, and are summarized in Table 3. Theoretical calculations were performed in the Gaussian 16 programme (Frisch et al. 2016) by combining density functional theory and the hybrid density functional B3LYP (Lee, Yang & Parr 1988; Becke 1992). The 6-311++ G(d,p) basis set was used for this system. The geometries of all species were optimized at the local minimum of their potential energy surface. Furthermore, the zero-point energy and thermal corrections obtained from the frequency calculations were used to correct the molecular energy.

Fig. 10 (A), after UV irradiation, $CH_4$ ice is converted into $CH_3$ through H-stripping and $CH_2$ through the loss of two H atoms or a $H_2$ molecule, that is, $CH_4 + h\nu \; CH \longrightarrow CH_3 + H$; $CH_4 + h\nu \longrightarrow CH_2 + 2H/H_2$. Similarly, pure $CD_4$ ice is converted into $CD_3$ through D-stripping during irradiation, i.e. $CD_4 + h\nu \longrightarrow CD_3 + D$. The H/D atoms produced from our experiments are 'hot' compared to the 'cold' H/D atoms (Ioppolo et al. 2008). And these 'hot' H/D atoms will further react with O-related species. Compared to other radicals, the diffusion barrier of 'hot' H/D atoms can be treated as zero, and their reactions with other radicals are extremely efficient.

In pure irradiated $CH_4$ ice, there are three photoproducts ($C_2H_6$, $C_2H_4$, and $C_3H_8$) with different reaction pathways. (1) $C_2H_6$ is formed by the reaction between the $CH_3$ radicals, i.e. $CH_3 + CH_3 \longrightarrow C_2H_6$. (2) $C_2H_4$ has two possible formation ways: one is through the reaction between $CH_2$ radicals, i.e. $CH_2 + CH_2 \longrightarrow C_2H_4$; the other is the dehydrogenation of $C_2H_6$, i.e. $C_2H_6 + h\nu \longrightarrow C_2H_4 + 2H/H_2$. (3) $C_3H_8$ has two possible formation ways: one is formed by the recombination between $CH_3$ and $CH_2$ radicals, i.e. $CH_3 + CH_2 \longrightarrow CH_3CH_2$, and then $CH_3CH_2 + CH_3 \longrightarrow C_3H_8$; the other is formed by the dehydrogenation of $C_2H_6$ and the recombination of radicals, i.e. $C_2H_6 + h\nu \longrightarrow CH_3CH_2 + H$, and then $CH_3CH_2 + CH_3 \longrightarrow C_3H_8$. In the irradiated pure $CD_4$ ice, only $C_2D_6$ is observed. Similarly, $C_2D_6$ is formed by the reaction between $CD_3$ radicals, i.e. $CD_3 + CD_3 \longrightarrow C_2D_6$.

In Fig. 10(B), similar to Zhen & Linnartz (2014), upon UV photolysis, O atoms and $O_3$ are the first generation products for pure $O_2$ ice, that is, $O_2 + h\nu \longrightarrow 2O$, $O_2 + O \rightleftarrows O_3$, and O and $O_3$ can transform into each other. Moreover, $O_3 \cdots O$ and $[O_3]_n$ ($n \geqslant 2$; e.g. $[O_3]_2$, $[O_3]_3$.....) could be produced by the reaction of $O_3$ with O and $O_3$, respectively, i.e. $O_3 + O \longrightarrow O_3 \cdots O$; $nO_3 \longrightarrow [O_3]_n$, n⩾2.

In Fig. 10(B), there are a series of photoproducts when $CH_4$:$O_2$ ice mixtures are exposed to UV photons, such as $H_2O$, $H_2O_2$, $CH_3OH$, $CH_2O$, CO, $CO_2$, HCOOH, $CH_3CH_2OH$, $CH_3CHO$, $O_3$, $O_3 \cdots O$, and $[O_3]_n$ ($n \geqslant 2$). In the irradiated mixed ices, there are two sources of radicals: (1) the $CH_3$ radicals and the hot 'H' atoms produced during the photodissociation process of the $CH_4$ ice are the first generation, and these hot 'H' atoms can diffuse freely in the ices; (2) energetic O-related radicals such as O atoms produced in the $O_2$ photodissociation are involved in further reactions. Subsequently, these atoms/radicals recombine with each other, and then new products are formed.

The formation reaction of each product shown in Fig. 10(B) is described in detail below. (1) $H_2O$ is formed by the reaction between the H atom and the OH radical, that is, $O + H \rightarrow OH$, $OH + H \rightarrow H_2O$. (2) $H_2O_2$ is formed by the combination of OH radicals, i.e. $2OH \rightarrow H_2O_2$. (3) $CH_3OH$ is formed by the reaction between $CH_3$ and OH radicals, that is, $CH_3 + OH \rightarrow CH_3OH$. (4) $CH_2O$ is formed by the dehydrogenation of $CH_3OH$, i.e. $CH_3OH + h\nu \rightarrow CH_2O + 2H/H_2$. Among the two reaction pathways, the reaction that produces $H_2$ is dominant. (5) CO is formed through the continuous dehydrogenation of $CH_2O$, i.e. $CH_2O + h\nu \rightarrow HCO + H$, $HCO + h\nu \rightarrow CO + H$. In this process, HCO radicals appear, react with other radicals, and form more complex species. (6) $CO_2$ is formed by the reaction between the O atom and CO, i.e. $CO + O \rightarrow CO_2$. (7) HCOOH is formed by the reaction between OH and the HCO radicals, that is, $HCO + OH \rightarrow HCOOH$. (8) $CH_3CH_2OH$ is formed by the reaction between $CH_3CH_2$ and OH radicals, i.e. $CH_3CH_2 + OH \rightarrow CH_3CH_2OH$. (9) $CH_3CHO$ is formed by the reaction between $CH_3$ and the HCO radicals, that is, $CH_3 + CHO \rightarrow CH_3CHO$.

Bergner et al. (2017) has studied the process of methanol formation through oxygen insertion chemistry in $CH_4$ ice. In their reaction

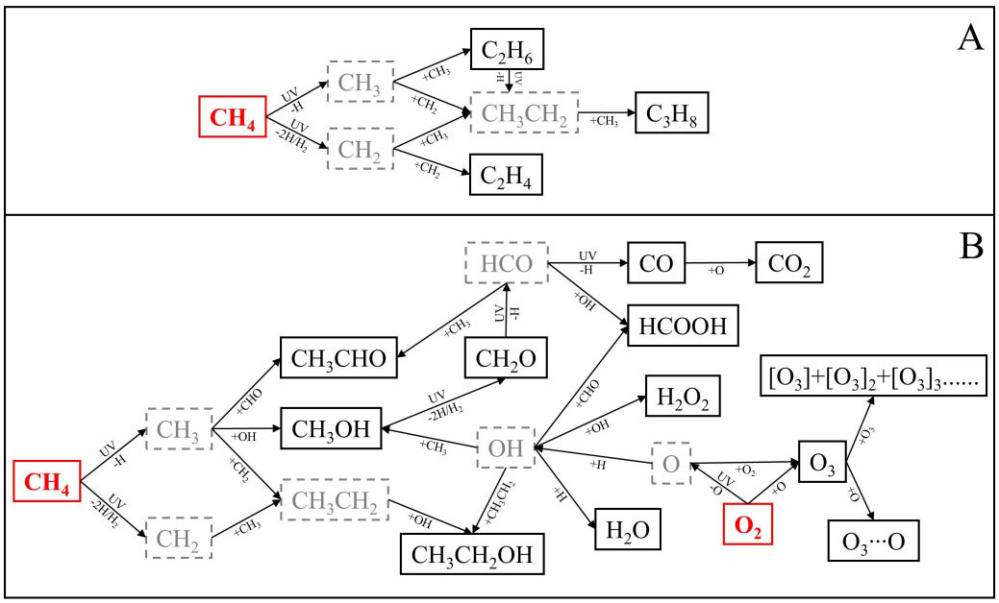


**Figure 10.** Reaction scheme of ice processing upon UV irradiation. (A) Pure $CH_4$ ice; (B) $CH_4$:$O_2$ ice mixtures. The solid boxes represent reactants and products, respectively, while the dotted boxes represent radicals.

**Table 3.** All reaction pathways and their reaction energies for the $CH_4$:$O_2$ system.

| No. | Reaction pathways | Reaction energy (eV) |
|---|---|---|
| 1 | $CH_4 \rightarrow CH_3 + H$ | 4.05 |
| 2 | $CH_4 \rightarrow CH_2 + 2H$ | 8.99 |
| 3 | $CH_4 \rightarrow CH_2 + H_2$ | 4.76 |
| 4 | $CH_3 + CH_3 \rightarrow C_2H_6$ | −3.30 |
| 5 | $CH_2 + CH_2 \rightarrow C_2H_4$ | −7.93 |
| 6 | $CH_3 + CH_2 \rightarrow CH_3CH_2$ | −4.40 |
| 7 | $CH_3CH_2 + CH_3 \rightarrow C_3H_8$ | −3.23 |
| 8 | $O_2 \rightarrow 2O$ | 3.34 |
| 9 | $O_2 + O \rightarrow O_3$ | −2.16 |
| 10 | $nO_3 \rightarrow [O_3] + [O_3]_2 + [O_3]_3$..... | – |
| 11 | $O_3 + O \rightarrow O_3 \cdots O$ | – |
| 12 | $O + H \rightarrow OH$ | −4.19 |
| 13 | $OH + H \rightarrow H_2O$ | −4.61 |
| 14 | $OH + OH \rightarrow H_2O_2$ | −1.65 |
| 15 | $CH_3 + OH \rightarrow CH_3OH$ | −3.40 |
| 16 | $CH_3OH \rightarrow CH_2O + 2H$ | 4.71 |
| 17 | $CH_3OH \rightarrow CH_2O + H_2$ | 0.48 |
| 18 | $CH_2O \rightarrow HCO + H$ | 3.35 |
| 19 | $HCO + OH \rightarrow HCOOH$ | −3.99 |
| 20 | $HCO \rightarrow CO + H$ | 0.70 |
| 21 | $CO + O \rightarrow CO_2$ | −5.35 |
| 22 | $CH_3 + CHO \rightarrow CH_3CHO$ | −3.14 |
| 23 | $CH_3CH_2 + OH \rightarrow CH_3CH_2OH$ | −3.47 |

network, $O_2$ is selectively dissociated through the channel $O_2 \longrightarrow O\,(^1D) + O\,(^3P)$, and then excited O ($^1$D) atoms are inserted into the methane, leading to the formation of methanol, i.e. $O\,(^1D) + CH_4 \longrightarrow CH_3OH$. Subsequently, the $CH_3$ and OH radicals are produced by the energetic processing of $CH_3OH$. Obviously, the formation mechanism of $CH_3OH$ is completely different from our analysis results. According to our analysis, the reason for this may be energetic processing; that is to say, different energetic processing for initial materials leads to the appearance of the same species with different production pathways.

Öberg et al. (2009a) quantifies the UV-induced production rates of complex organics in $CH_3OH$-rich ices (e.g. pure $CH_3OH$ ice or $CH_3OH$:$CH_4$/CO ice mixtures). $C_2H_6$, $CH_3CHO$, $CH_3CH_2OH$, $CH_3OCH_3$, $HCOOCH_3$, $HOCH_2CHO$, and $(CH_2OH)_2$ are detected in their experiments. Mejía et al. (2013) has studied the radiolysis of pure methane ice with 6−606 MeV heavy ions (i.e. O, Fe, and Zn) at 15 K, leading to the formation of $C_nH_m$ molecules ($n$ = 2–4 and $m = 2(n-1)$ to $2(n+1)$) and some radicals $CH_3$, $C_2H_3$, and $C_2H_5$. More complex molecules are obtained under cosmic-ray radiation, while only $C_2H_4$, $C_2H_6$, and $C_3H_8$ molecules are formed through interaction between pure $CH_4$ ice and UV photons in our experiments. This indicates that radiation sources with different energies affect the types of photoproducts. In addition, physico-chemical modification of $CH_4$:$H_2O$ ice mixtures irradiated by 40 MeV $^{58}Ni^{11+}$ ions are analysed (Mejía et al. 2020). New molecules appear in the irradiated $CH_4$:$H_2O$ ices, such as HCO, $H_2CO$, CO, $CO_2$, $H_2O_2$, HCOOH, $CH_3OH$, $C_2H_5OH$, and $CH_3CHO$, which are also observed in this work. More importantly, these products have a similar formation mechanism under different radiation sources. These similarities indicate that UV photolysis can produce a rich chemistry comparable to ion-induced radiolysis.

Qualitatively, the relative production rates of $CH_3OH$, $CH_2O$, $H_2O$, $O_3$, CO, and $CO_2$ agree well with the normalized formation rates observed according to the prediction of their reaction scheme. Within this framework, it is assumed that most reactions consist of radical recombination without breaking chemical bonds. This scheme reproduces the true and complex chemistry in interstellar ice in the star-formation regions as well.

## 6 ASTROPHYSICAL IMPLICATION

The prospect of reactive species such as ozone in cold and dense molecular clouds is particularly interesting because the O atom is a key starting point for multiple routes of molecular synthesis. As our experimental results are presented here, $CH_4$:$O_2$ ice mixtures upon UV irradiation result in a series of complex organic molecules. During the different stages of star formation, the relative importance

of these production pathways strongly depends on the relative abundances of $CH_4$ and $O_2$ ice on the surface of dust grains, as well as what they are mixed with, e.g. other ice compounds, UV photons, and cosmic ray particles. Therefore, both the $H_2O$- and $CO/CH_3OH$-rich ice phases can be accurately modelled and thus predict the formation rates of complex C- and/or O-containing molecules from interstellar space.

The ice lifetime in the radiation field could easily be estimated through the photodestruction cross-section of volatile species (e.g. $CH_4$). The photodestruction time-scales of $CH_4$ in mixed ices subject to a weak UV field induced by cosmic rays ($10^4\,cm^{-2}\,s^{-1}$): $\sim 1.0 \times 10^7$ yrs, the interstellar radiation field ($10^8\,cm^{-2}\,s^{-1}$): $\sim 1.0 \times 10^3$ yrs, and the 1000 times higher UV flux inferred toward the L1527 outflow ($10^{11}\,cm^{-2}\,s^{-1}$): $\sim$1 yr (Spaans et al. 1995). Inside a cloud core with low temperatures and lots of molecular hydrogen, $CH_4$ ices are well protected so that they can survive thermal desorption and irradiation around some protostars and drive warm-carbon-chain chemistry (Sakai et al. 2008). This may be a reason for the low number of chemical observations on protostellar evolution.

$O_2$ condensed in the dust grains can be partially converted into ozone by energetic cosmic rays or UV radiation. So far, though the observation results have been negatived for the presence of $O_3$ on the surface of dust grains, the ozone absorption band at 9.6 μm may be obscured by a broad absorption characteristic attributed to silicates or other carbonaceous materials at 10.0 μm. Photodissociation of ozone could produce O atoms that could react with other molecules, such as CO, to produce $CO_2$, possibly assisted by localized energy deposition. If the above process is relevant, it could help resolve the problem of accounting for the observed abundance of solid $CO_2$ in interstellar clouds. Throughout protostars, the potential importance of producing complex organics from simple ices containing $O_2$ and/or $CH_4$ should therefore be taken into account in the simulation of ice chemistry.

Given the low temperatures in dense molecular clouds, interstellar ice processing is mainly driven by non-thermal processes such as energetic processing caused by UV photons. For the astrophysically relevant ice analogues, $CH_4$ is at the beginning of a rich chemistry network. Furthermore, O is also one of the essential elements of life. Therefore, the research about $CH_4$:$O_2$ ice mixtures plays an important role in the development of iCOMs, amino acids, and even life. Laboratory experiments about photochemistry behaviour induced by UV irradiation help explain the astronomical observations of molecule abundances in the gas and solid phases and to accurately model the chemical evolution in the regions of the ISM/CSM concerned.

## 7 CONCLUSION

In total, UV-induced photochemical processes for $CH_4$:$O_2$ ice mixtures have been studied by experimental simulation and quantitative analysis. The results reveal an efficient way to form complex organic species under astronomically relevant conditions.

The main conclusions we obtained are summarized below: (1) After UV irradiation, all new species formed in the mixed ices are identified through mid-IR spectra. These species, including $CH_2O$, $CH_3OH$, $O_3$, CO, $CO_2$, $H_2O$, $H_2O_2$, HCOOH, $CH_3CH_2OH$, and $CH_3CHO$, and the D-products $CD_3OD$, HDCO, $D_2O$, and $CD_2O$, play a crucial role in the formation of complex organic species.

(2) The photodestruction cross-sections of $CH_4$ and $CD_4$ in pure and mixed ices are obtained under different experimental and astronomically relevant conditions;

(3) The formation rates of $O_3$, $H_2O$, $CH_3OH$, $CH_2O$, and CO are quantified, and thus they can be used directly for theoretical models, such as those related to the chemical evolution of the interstellar medium, under astronomically relevant conditions.

(4) Together with the experiments and quantitative analysis, we have derived the reaction scheme of $CH_4$: $O_2$ ice mixtures upon UV irradiation and provided the expected main reaction pathways under simulated astrophysical environmental conditions.

Our results also indicate that organic molecules can form and accumulate on the surface of small dust grains in the ISM/CSM, which helps to understand the formation of large organic molecules through the photochemical evolution of simple ices in the ISM/CSM.

## ACKNOWLEDGEMENTS

This work was supported by the National Natural Science Foundation of China (NSFC, grant no. 12333005). Theoretical calculations were performed at the Super Computing Center of the University of Science and Technology of China.

## DATA AVAILABILITY

All data generated and analysed during this work are included in this article.

## REFERENCES

Asplund M., Grevesse N., Sauval A. J., Scott P., 2009, ARA&A, 47, 481
Barentine J. C., Lacy J. H., 2012, ApJ, 757, 111
Becke A. D., 1992, J. Chem. Phys., 96, 2155
Bennett C. J., Jamieson C. S., Osamura Y., Kaiser R. I., 2005, ApJ, 624, 1097
Bennett C. J., Jamieson C. S., Osamura Y., Kaiser R. I., 2006, ApJ, 653, 792
Bennett C. J., Chen S. H., Sun B. J., Chang A. H., Kaiser R. I., 2007, ApJ, 660, 1588
Bergner J. B., Öberg K. I., Rajappan K. I., 2017, ApJ, 845, 29
Boogert A. C. A. et al., 1996, A&A, 315, L377
Boogert A. C., Schutte W. A., Helmich F. P., Tielens A. G., Wooden D. H., 1997, A&A, 317, 929
Boogert A. C., Helmich F. P., Dishoeck E. F. V., Schutte W. A., Tielens A. G. G. M., Whittet D. C. B., 1998, A&A, 336, 352
Boogert A. C. A., Blake G. A., Tielens A. G. G. M., 2002, ApJ, 577, 271
Boogert A. C. A., Blake G. A., Öberg K., 2004, ApJ, 615, 344
Boogert A. C. A., Gerakines P. A., Whittet D. C. B., 2015, ARA&A, 53, 541
Bossa J. B., Paardekooper D. M., Isokoski K., Linnartz H., 2015, Phys. Chem. Chem. Phys., 17, 17346
Brewer L., Wang J. L., 1972, J. Chem. Phys., 56, 759
Carrascosa H., Cruz-Díaz G. A., Muñoz Caro G. M., Dartois E., Chen Y., 2020, MNRAS, 493, 821
Chen J. H. et al., 2014, ApJ, 793, 111
Chiar J. E., Tielens A. G. G. M., Whittet D. C. B., Schutte W. A., Boogert A. C. A., Lutz D., van Dishoeck E. F., Bernstein M. P., 2000, ApJ, 537, 749
Chou S., Lin M., Huang T., Wu Y., 2020, J. Mol. Struct., 1209, 127954
Cottin H., Moore M. H., Bénilan Y., 2003, ApJ, 590, 874
Dartois E., Muñoz Caro G. M., Deboffle D., Montagnac G., d'Hedecourt L., 2005, A&A, 432, 895
de Barros A. L. F., Domaracka A., Andrade D. P. P., Boduch P., Rothard H., da Silveira E. F., 2011, MNRAS, 418, 1363
de Barros A. L. F., da Silveira E. F., Pilling S., Domaracka A., Rothard H., Boduch P., 2014, MNRAS, 438, 2026
de Graauw T. D. et al., 1996, A&A, 315, L49
Dupuy R. et al., 2017, A&A, 603, A61
Ehrenfreund P., Charnley S. B., 2000, ARA&A, 38, 427
Faggi S., Lippi M., Mumma M. J., Villanueva G. L., 2023, Planet. Sci. J., 4, 8
Freiman Y. A., Jodl H. J., 2004, Phys. Rep., 401, 1

Frisch M. J. et al., 2016, Gaussian 16, Revision e. 01. Gaussian, Inc., Wallingford, CT
Garrod R. T., Wakelam V., Herbst E., 2007, A&A, 467, 1103
Gerakines P. A., Schutte W. A., Greenberg J. M., van Dishoeck E. F., 1995, A&A, 296, 810
Gerakines P. A., Schutte W. A., Ehrenfreund P., 1996, A&A, 312, 289
Gibb E. L., Whittet D. C. B., Chiar J. E., 2001, ApJ, 558, 702
Goldsmith P. F. et al., 2011, ApJ, 737, 96
Greenberg J. M., Hong S. S., 1974, Proc. IAU Symp. 60, Galactic Radio Astronomy. Cambridge Univ. Press, Cambridge, p. 155
Herbst E., Leung C. M., 1989, ApJS, 69, 271
Hidaka H., Watanabe M., Kouchi A., Watanabe N., 2009, ApJ, 702, 291
Ioppolo S., Cuppen H. M., Romanzin C., van Dishoeck E. F., Linnartz H., 2008, ApJ, 686, 1474
Kerkhof O., Schutte W. A., Ehrenfreund P., 1999, A&A, 346, 990
Lacy J. H., Carr J. S., Evans Neal J., II, Baas F., Achtermann J. M., Arens J. F., 1991, APJ, 376, 556
Lamberts T., de Vries X., Cuppen H. M., 2014, Faraday Discuss., 168, 327
Lamberts T., Fedoseev G., Kästner J., Ioppolo S., Linnartz H., 2017, A&A, 599, A132
Larsson B., Liseau R., 2017, A&A, 608, A133
Larsson B. et al., 2007, A&A, 466, 999
Lee C., Yang W., Parr R. G., 1988, Phys. Rev. B, 37, 785
Liseau R. et al., 2012, A&A, 541, A73
Markwick A. J., Millar T. J., Charnley S. B., 2000, ApJ, 535, 256
McClure M. K. et al., 2023, Nat. Astron., 7, 431
Mejía C. F., de Barros A. L. F., Bordalo V., da Silveira E. F., Boduch P., Domaracka A., Rothard H., 2013, MNRAS, 433, 2368
Mejía C. F., de Barros A. L. F., Rothard H., Boduch P., da Silveira E. F., 2020, ApJ, 894, 132
Millar T. J., Herbst E., 1990, MNRAS, 242, 92
Moore M. H., Hudson R. L., 1998, Icarus, 135, 518
Muñoz Caro G. M., Schutte W. A., 2003, A&A, 412, 121
Nickerson S. et al., 2023, ApJ, 945, 26
Öberg K. I. et al., 2008, ApJ, 678, 1032
Öberg K. I., Garrod R. T., van Dishoeck E. F., Linnartz H., 2009a, A&A, 504, 891
Öberg K. I., Linnartz H., Visser R., van Dishoeck E. F., 2009b, ApJ, 693, 1209
Öberg K. I., van Dishoeck E. F., Linnartz H., 2009c, A&A, 496, 281
Pontoppidan K. M. et al., 2003, A&A, 408, 981
Raut U., Loeffler M. J., Fama M., Baragiola R. A., 2011, J. Chem. Phys., 134, 194501
Sakai N., Sakai T., Hirota T., Yamamoto S., 2008, ApJ, 672, 371
Savage B. D., Sembach K. R., 1996, ARA&A, 34, 279
Schutte W. A., Allamandola L. J., Sandford S. A., 1993, Icarus, 104, 118
Shen C. J., Greenberg J. M., Schutte W. A., van Dishoeck E. F., 2004, A&A, 415, 203
Shimanouchi T., 1972, Tables of Molecular Vibrational Frequencies, Consolidated Volume I, National Bureau of Standards. NSRDS-NBS, US, p. 164
Spaans M., Hogerheijde M. R., Mundy L. G., van Dishoeck E. F., 1995, ApJ, 455, L167
Spoon H. W. W., Keane J. V., Tielens A. G. G. M., Lutz D., Moorwood A. F. M., 2001, A&A, 365, L353
Taquet V. et al., 2018, A&A, 618, A11

**Table A1.** The corresponding parameters of fitting lines in Fig. 5(B).

| | $C_2H_6$ (2941 $cm^{-1}$) |
|---|---|
| Fitting model | Exponential decay |
| Functional equation | $y = A_1 \times \exp(-x/t_1) + y_0$ |
| $y_0$ | 0.02471 ± 0.00328 |
| $A_1$ | −0.0237 ± 0.00309 |
| $t_1$ | 190.0166 ± 40.25831 |
| Reduced chi-sqr | 0.39686 |
| $R^2$ (COD) | 0.98039 |
| Adjusted $R^2$ | 0.97899 |
| | $C_2H_4$ (1436 $cm^{-1}$) |
| Fitting model | Exponential decay |
| Functional equation | $y = A_1 \times \exp(-x/t_1) + y_0$ |
| $y_0$ | 0.00907 ± 0.0073 |
| $A_1$ | −0.00902 ± 0.00723 |
| $t_1$ | 490.90089 ± 472.64426 |
| Reduced chi-sqr | 0.04667 |
| $R^2$ (COD) | 0.93898 |
| Adjusted $R^2$ | 0.93463 |
| | $C_3H_8$ (2959 $cm^{-1}$) |
| Fitting model | Logistic function |
| Functional equation | $y = A_2 + (A_1\text{-}A_2)/(1 + (x/x_0)^p)$ |
| $A_1$ | −7.84891E-5 ± 3.56745E-4 |
| $A_2$ | 0.03892 ± 0.0519 |
| $x_0$ | 305.47495 ± 343.30285 |
| $p$ | 1.824 ± 0.53356 |
| Reduced chi-sqr | 0.50735 |
| $R^2$ (COD) | 0.96084 |
| Adjusted $R^2$ | 0.95649 |

van Dishoeck E. F., Wright C. M., Cernicharo J., González-Alfonso E., de Graauw T., Helmich F. P., Vandenbussche B., 1998, ApJ, 502, L173
van Dishoeck E. F., Herbst E., Neufeld D. A., 2013, Chem. Rev., 113, 9043
Vandenbussche B. et al., 1999, A&A, 346, L57
Wakelam V., Herbst E., Selsis F., 2006, A&A, 451, 551
Whittet D. C. B., Bode M. F., Longmore A. J., Adamson A. J., McFadzean A. D., Aitken D. K., Roche P. F., 1988, MNRAS, 233, 321
Yildiz U. A. et al., 2013, A&A, 558, A58
Zhen J., Linnartz H., 2014, MNRAS, 437, 3190

## APPENDIX: FITTING MODELS

Non-linear regression models were applied to all scatter plots in Figs 5(B) and 7. In Fig. 5(B), $C_3H_8$ (2959 $cm^{-1}$) data were modelled using a logistic function, with the functional form of $y = A_2 + (A_1 - A_2)/(1 + (x/x_0)^p)$. Except for $C_3H_8$, other data sets in Fig. 5(B) were modelled using an exponential decay model, with the functional form of $y = A_1 \times \exp(-x/t_1) + y_0$. In Fig. 7, all the data sets were modelled using an exponential growth model, with the functional form of $y = A_1 \times \exp(x/t_1) + y_0$. The corresponding best-fitting parameters are shown in Table A1 and A2.

**Table A2.** The corresponding parameters of fitting lines in Fig. 7.

| | 60 ML, 14 K, $O_2$ |
|---|---|
| Fitting model | Exponential growth |
| Functional equation | $y = A_1 \times \exp(x/t_1) + y_0$ |
| $y_0$ | 9.14875 ± 0.1121 |
| $A_1$ | −8.2639 ± 0.19845 |
| $t_1$ | −1.80333E17 ± 1.04155E16 |
| Reduced chi-sqr | 0.06166 |
| $R^2$ (COD) | 0.99108 |
| Adjusted $R^2$ | 0.98996 |
| | 50 ML, 14 K, $CD_4$:$O_2$ = 1:1 |
| Fitting model | Exponential growth |
| Functional equation | $y = A_1 \times \exp(x/t_1) + y_0$ |
| $y_0$ | 1.82732 ± 0.04056 |
| $A_1$ | −1.80093 ± 0.18406 |
| $t_1$ | −3.55564E16 ± 7.35532E15 |
| Reduced chi-sqr | 0.03409 |
| $R^2$ (COD) | 0.82448 |
| Adjusted $R^2$ | 0.80922 |
| | 40 ML, 14 K, $CH_4$:$O_2$ = 1:1 |
| Fitting model | Exponential growth |
| Functional equation | $y = A_1 \times \exp(x/t_1) + y_0$ |
| $y_0$ | 1.09504 ± 0.07807 |
| $A_1$ | −1.06116 ± 0.38338 |
| $t_1$ | −1.91557E16 ± 1.68524E16 |
| Reduced chi-sqr | 0.14828 |
| $R^2$ (COD) | 0.25796 |
| Adjusted $R^2$ | 0.1986 |

This paper has been typeset from a TEX/LATEX file prepared by the author.